Supporting Information for:

Characterization of an Fe≡N-NH$_2$ Intermediate Relevant to Catalytic N$_2$ Reduction to NH$_3$

John S. Anderson[†ε], George E. Cutsail III[‡ε], Jonathan Rittle[†ε], Bridget A. Connor[†], William A. Gunderson[‡#], Limei Zhang[†§*], Brian M. Hoffman[‡*], Jonas C. Peters[†*]

[†]Division of Chemistry and Chemical Engineering, California Institute of Technology, Pasadena, California 91125, United States

[‡]Department of Chemistry, Northwestern University, 2145 Sheridan Road, Evanston, Illinois 60208, United States

[§] Current address: Department of Biochemistry and Redox Biology Center, University of Nebraska-Lincoln, Lincoln, NE 68588, United States

[#] Current address: Department of Chemistry, Illinois College, 1101 West College Avenue, Jacksonville, IL, 62650, United States

Email: jpeters@caltech.edu, bmh@northwestern.edu, limei.zhang@unl.edu

General Considerations. Unless otherwise noted, all compounds were purchased from commercial sources and used without further purification. $[(TPB)Fe(N_2)][Na(12\text{-crown-}4)_2]$,[1] $(TPB)Fe(N_2)$,[1] $HBAr^F_4 \cdot 2\ Et_2O$,[2] $[Cp_2Fe][BAr^F_4]$,[3] and KC_8,[4] were prepared according to literature procedures ($[BAr^F_4] = [(3,5\text{-}(CF_3)_2\text{-}C_6H_3)_4B]^-$) . All manipulations were carried out under an N_2 atmosphere utilizing standard glovebox or Schlenk techniques. Solvents were dried and de-oxygenated by an argon sparge followed by passage through an activated alumina column purchased from S.G. Waters Company. Labeled $^{15}N_2$ (98% purity) was obtained from Cambridge Isotope Laboratories.

EPR Spectroscopy. EPR X-band spectra were obtained on a Bruker EMX spectrometer with the aid of Bruker Win-EPR software suite version 3.0. The spectrometer was equipped with a rectangular cavity which operated in the TE_{102} mode. Temperature control was achieved with the use of an Oxford continuous-flow helium cryostat (temperature range 3.6 – 300 K). All spectra were recorded at 9.37 GHz with a microwave power of 2 mW, a modulation amplitude of 4 G, and a modulation frequency of 100 kHz. Simulations were performed with the Easyspin software suite.[5] EPR samples were thawed to -40 °C with a dry ice/acetonitrile slush bath for a time period of 5 minutes or alternately thawed to room temperature for a time period of 5 minutes. Spin integration was performed in triplicate by preparing samples of **2** as described below. Integration was performed by doubly integrating the signal from **2** and comparing the resulting values to those from a solution of **1** with identical [Fe], volume, and scan parameters. The three runs provided values of 90%, 78%, and 92% for an average yield of 87(8)%.

EXAFS Measurements. The extended X-ray absorption fine structure (EXAFS) data collection was conducted at the Stanford Synchrotron Radiation Laboratory (SSRL) with the SPEAR 3 storage ring containing 500 mA at 3.0 GeV. Fe K-edge data were collected on the beamline 9-3 operating with a wiggler field of 2 T and employing a Si(220) double-crystal monochromator. Beamline 9-3 is equipped with a rhodium-coated vertical collimating mirror upstream of the monochromator and a bent-cylindrical focusing mirror (also rhodium-coated) downstream of the monochromator. Harmonic rejection was accomplished by setting the energy cutoff angle of the mirrors to 10 keV. The incident and transmitted X-ray intensities were monitored using Nitrogen-filled ionization chambers, and X-ray absorption was monitored by measuring the Fe Kα fluorescence intensity using an array of 100 Canberra germanium detectors. During data collection, samples were maintained at a temperature of approximately 10 K using an Oxford instruments liquid helium flow cryostat. The energy was calibrated by reference to the absorption of a standard iron metal foil measured simultaneously with each scan, assuming a lowest energy inflection point of the iron foil to be 7111.2 eV.

The EXAFS oscillations $\chi(k)$ were quantitatively analyzed by non-linear least square curve-fitting using the EXAFSPAK suite of computer programs.[6] Ab-initio theoretical phase and

amplitude functions were calculated using the program FEFF version 8.[7] No smoothing, filtering, or related operations were performed on the data.

Computational Methods. Geometry optimizations were performed using the Gaussian03 or the Gaussian09 packages.[8,9] The BP86 exchange-correlation functional was employed with a 6-31G(d) basis set on Fe, P, N, and B and the 6-31G basis set on C and H for the Gaussian03 calculations. Alternately, the M06L functional with the TZVP basis set on Fe, the SVP basis set on P, B, and N, and the 6-31G basis set on C and H. A full frequency calculation was performed on each structure to establish true minima. The initial geometries used for the calculations were the XRD coordinates for [(TPB)Fe≡NAd][BAr^F_4] which was modified to feature the correct nitrogenous ligands. Computed energies were corrected for thermal energy. Structural models were generated as .mol files and plotted in Diamond 3.2 and orbital/spin density pictures were generated from GaussView 03.

Synthesis of [(TPB)Fe≡N-NH_2][BAr^F_4], 2. Complex **1** (4 mg, 0.004 mmol) was dissolved in 2-MeTHF (0.25 mL) and added into a quartz EPR tube. This solution was then frozen in a liquid N_2 cooled cold well. A thawing solution of $HBAr^F_4 \cdot 2\ Et_2O$ (38 mg, 0.037 mmol) in 2-MeTHF (0.25 mL) was then added to the EPR tube and frozen before reaching the bottom of the tube. A long needle, which had also been cooled to 77K, was then inserted into the tube and used to mechanically mix the solutions as thawing gels over 10 minutes. The tube was also raised slightly out of the cold well to slightly thaw the solutions and aid in mixing. After mixing was complete, the dark red color of **1** had disappeared and a brown yellow solution was obtained. This frozen tube solution was then brought out of the glovebox and subjected to EPR analysis.

Synthesis of (TPB)Fe≡N-Ad. Under an atmosphere of nitrogen, a 0.09 M solution of adamantyl azide in benzene (1.7 mL, 0.148 mmol) was added to a solution of (TPB)Fe(N_2) (90 mg, 0.133 mmol) in benzene (5 mL) and stirred, giving a deep red solution. The solution was transferred to a sealed Schlenk tube and stirred overnight at 80 °C resulting in a deep green solution. Lyophilization yielded a green powder which was washed twice in THF leaving a bright green powder ((TPB)Fe≡N-Ad) (58 mg, 0.073 mmol, 55%). The product was suspended in benzene and lyophilized in preparation for elemental analysis. Elemental analysis yielded the following results: Calculated: C 69.44, H 8.74, N 1.76; Experimental: C 69.29, H 8.47, N 1.67. NMR and UV-Vis analysis were not obtained due to the poor solubility properties of the product.

Synthesis of [(TPB)Fe≡N-Ad][BAr^F_4], 4. A solution of (TPB)Fe≡N-Ad (12.5 mg, 0.015 mmol) in THF (3 mL) was added to a solution of [$FeCp_2$][BAr^F_4] (16.5 mg, 0.015 mmol) in THF (2 mL) giving a dark green solution which was stirred for 15 minutes. The solvent was removed, leaving a dark green sludgy solid [(TPB)Fe≡N-Ad][BAr^F_4] which was washed three times in pentane. Crystals of [(TPB)Fe≡N-Ad][BAr^F_4] (13.5 mg, 0.008 mmol, 53%) for XRD were obtained by vapor diffusion of pentane into a solution of [(TPB)Fe≡N-Ad][BAr^F_4] in diethyl ether. ^{1}H NMR (THF-d_8, δ): 26.56 (vbr s), 10.66 (br s), 7.77 (s, $BAr^F_4{}^-$), 7.69 (br s), 7.56 (s, $BAr^F_4{}^-$), 6.67 (vbr s), 6.48 (br s), 5.44 (br s), 4.96 (br s), 3.16 (br s), -2,85 (vbr s), −5.96 (br s), -

6.53 (br s), -8.23 (vbr s), -13.96 (br s). Solution magnetic moment (THF-d_8): 3.9 μ_B. UV-Vis (THF) λ_{max}, nm: 655. Anal. calcd. for $C_{78}H_{81}B_2F_{24}FeNP_3$: C 56.48 , H 4.92, N 0.84; found: C 56.24, H 4.83, N 0.80.

Oxidation of (TPB)Fe(N_2) with acid. A suspension of (TPB)Fe(N_2) (20 mg, 0.030 mmol) in Et_2O (3 mL) was cooled to -78 °C in a dry ice/acetone cooled cold well. A similarly cooled solution of $HBAr^F_4 \cdot 2\ Et_2O$ (30 mg, 0.030 mmol) in Et_2O was then added to the suspension of (TPB)Fe(N_2) with stirring. The mixture was allowed to stir at -78 °C for 10 minutes before being warmed to room temperature and stirred for an additional 2 hours. As it warmed the mixture became homogenous and lightened in color to provide an orange solution. The solution was then concentrated to 1.5 mL and subjected to a pentane vapor diffusion at -35 °C. The product [(TPB)Fe][BAr^F_4] was obtained as a dark orange crystalline material (42 mg, 0.028 mmol, 93%). The spectroscopic signatures of [(TPB)Fe][BAr^F_4] were identical to those previously reported.[10]

Preparation of ENDOR samples. Samples of **1** were prepared by dissolving the complex (1.2 mg, 0.001 mmol) in 2-MeTHF (0.5 mL) and transferring this solution to an ENDOR tube before freezing the solution prior to shipping. Samples of **2** were prepared analogously as described above with **1** (1 mg, 0.0009 mmol) and $HBAr^F_4 \cdot 2\ Et_2O$ (10 mg, 0.0099 mmol) in 2-MeTHF (total volume of 0.5 mL). The only deviation from the above described procedure was that **2** was initially prepared in a 5 mL scintillation vial before being slightly thawed and transferred into the ENDOR tube while cold. The samples were then frozen and packaged for shipment. They were shipped to Northwestern University under liquid N_2.

Preparation of ^{15}N labeled ENDOR samples. Two stock solutions of **1** (5 mg, 0.0048 mmol) and $HBAr^F_4 \cdot 2\ Et_2O$ (50 mg, 0.049 mmol) in 2-MeTHF (0.5 mL each) and 2-MeTHF (1 mL) were each placed into 3 short test tubes. These test tubes and the ENDOR tubes were placed into a round-bottom Schlenk flask with a glass stopcock side-arm. The flask was then sealed with a rubber septum and brought out of the glovebox. The solution was freeze-pump-thawed 3x before backfilling with an atmosphere of $^{15}N_2$. The solutions were then sparged with $^{15}N_2$ from the headspace of the flask with the use of a long needled syringe through the rubber septum. The syringe was rinsed with the 2-MeTHF from the third test tube to avoid cross contamination. The solution of **1** was then distributed to the ENDOR tubes with the use of the syringe. To generate **2**, the apparatus was cooled to 77 K with liquid nitrogen. The solutions were then briefly thawed and the solution of $HBAr^F_4 \cdot 2\ Et_2O$ was layered on top of the solutions of **1** in the ENDOR tubes. The solutions were then mechanically mixed with the syringe needle as described above. After mixing was complete, the solutions were frozen, and the septum was removed after which the samples were quickly dumped into liquid N_2 before being sealed for shipment. The samples were shipped to Northwestern University under liquid N_2.

Preparation of XAS samples. The sample of **2** for XAS analysis was prepared analogously to that reported earlier with **1** (10 mg, 0.0095 mmol) and $HBAr^F_4 \cdot 2\ Et_2O$ (100 mg, 0.099 mmol) in 2-MeTHF (0.5 mL total volume). The solution was prepared in a 5 mL scintillation vial before

being slightly thawed and transferred into the XAS sample holder with a syringe. While care was taken to keep the sample as cold as possible during these manipulations, the required thawing of the solution for syringe transfer likely raised the temperature of the solution substantially. The sample was then re-frozen before being packaged for shipping to SSRL. The sample was shipped under liquid N_2.

Preparation and EPR analysis of 2 at -78 °C. Complex **1** (8 mg, 0.0076 mmol) was suspended in Et_2O (0.25 mL) and cooled to -78 °C in a 5 mL scintillation vial. $HBAr^F_4 \cdot 2\ Et_2O$ (80 mg, 0.079 mmol) was dissolved in Et_2O (0.25 mL) in a 20 mL scintillation vial equipped with a stir bar and cooled to -78 °C as well. Once cooled, the suspension of **1** was added to the $HBAr^F_4 \cdot 2\ Et_2O$ with stirring. The resulting solution was dark yellow-brown and homogeneous and was allowed to stir at -78 °C for 10 minutes. To this solution was then added 2-MeTHF (0.5 mL) which had been similarly cooled to -78 °C. The resulting solution was then transferred into an EPR tube and frozen with liquid N_2 before analysis.

EPR analysis of the reaction of complex 1 with one equivalent of $HBAr^F_4 \cdot 2\ Et_2O$. The procedure employed was identical to that used for the generation of **2** with the exception that only one equivalent of $HBAr^F_4 \cdot 2\ Et_2O$ (3.8 mg, 0.0038 mmol) was used.

Preparation and Interpretation of Mössbauer Analysis of 2. A 500 μL aliquot of $[(TPB)^{57}Fe(N_2)][Na(Et_2O)_x]$ (5 mM, Et_2O) was frozen in a 5 mL scintillation vial inside of a cold well chilled to 77 K. A 500 μL aliquot of chilled $HBAr^F_4 \cdot 2\ Et_2O$ (25 mM, Et_2O) was subsequently layered on top of the Fe-containing layer and frozen. The vial was elevated off of the cold well floor with pre-chilled forceps and the mixture subsequently began to melt (T ~ -110 ^oC). To facilitate rapid mixing at the lowest possible temperature, the two layers were mechanically stirred with a similarly cooled spatula. The dark orange-red color of $[(TPB)^{57}Fe(N_2)][Na(Et_2O)_x]$ rapidly bleached on mixing and was replaced with a light yellow-green color. This solution was subsequently chilled to near-freezing before being poured into a Mössbauer sample cup chilled to 77 K.

The 80 K ^{57}Fe Mössbauer spectrum of the resulting mixture is shown in Figure 3 of the main text and reprinted for clarity in Figure S4A of the supporting information. This spectrum was collected in the presence of a 50 mT magnetic field, which served to sharpen quadrupole doublets associated with $S = 1/2$ species (*vide infra*). Six distinct features of similar intensity are observed, suggesting the presence of multiple Fe-containing species. Similarly prepared samples show these features in varying ratios, eliminating the possibility that the six features arise from a single Fe species. ^{57}Fe Mössbauer spectra of independently prepared samples of $(TPB)^{57}Fe(N_2)$, $[(TPB)^{57}Fe][Bar^F_4]$, and $[(TPB)^{57}Fe(N_2)][Na(Et_2O)_x]$ in frozen Et_2O solutions are shown in Figure S5 of the supporting information and their parameters are tabulated in Table S1.

At 80 K, $[(TPB)Fe{\equiv}N\text{-}NH_2][BAr^F_4]$ and $[(TPB)^{57}Fe(N_2)][Na(Et_2O)_x]$ are slowly-relaxing Kramers systems, as evidenced by the EPR signatures observed at this temperature. At

sufficiently low temperatures, this magnetic interaction may serve to broaden and/or split the quadrupole doublet features associated with these species in their Mössbauer spectra. To establish conditions wherein this magnetic hyperfine interaction is minimized, Mössbauer spectra of $[(TPB)^{57}Fe(N_2)][Na(Et_2O)_x]$ were collected under a variety of conditions (Figure S6).

At temperatures lower than 20 K, a broadened spectrum consisting of at least four features is observed. At 80 K in the absence of an applied magnetic field, a broad, asymmetric quadrupole doublet is observed, displaying the onset of slow magnetic relaxation. Application of a 50 mT magnetic field at this temperature sharpens this quadrupole doublet, and removes most of the asymmetry. Under these conditions (80 K, 50 mT applied field) we anticipate that $[(TPB)Fe{\equiv}N\text{-}NH_2][BAr^F{}_4]$ will also display a relatively sharp quadrupole doublet.

To deconvolute the mixture of species obtained from low temperature protonation of $[(TPB)^{57}Fe(N_2)][Na(Et_2O)_x]$, we initially assumed that a finite quantity of the 1-electron oxidized congener, $(TPB)Fe(N_2)$, would be present. $(TPB)Fe(N_2)$ has a signature large quadrupole splitting (3.34 mm/s) that produces features at greater velocities than $[(TPB)^{57}Fe][Bar^F{}_4]$ or $[(TPB)^{57}Fe(N_2)][Na(Et_2O)_x]$. Therefore the presence of $(TPB)Fe(N_2)$ is easily discerned and its presence in the mixture is highlighted by the two red lines in Figure S4A. $(TPB)Fe(N_2)$ constitutes ca. 19% of the total Fe content of this sample and subtraction of its features produces the spectrum shown in Figure S4B. Four distinct features remain in this spectrum. Unfortunately, each of these features has roughly equal integrals, and three different simulations produce nearly equivalent fits to the data. The three simulations are shown in Figure S7 and the resulting parameters are tabulated in Table S2.

Inspection of the hyperfine parameters obtained for the simulation shown in Figure S7C suggests that this solution is unlikely. The isomer shift values, (δ = -0.32 and 1.38) are unreasonably small/large for known Fe compounds supported by the TPB ligand, and we hence discarded this solution. While the hyperfine parameters obtained in the simulation shown in Figure S7B are not unreasonable (δ = 0.19, 0.87 mm/s) we have thus far not obtained Mössbauer spectra on (TPB)Fe compounds that display isomer shift values higher than 0.8 mm/s. We favor the simulation shown in Figure S7A, as one component displays very similar hyperfine parameters to $[(TPB)Fe][BAr^F{}_4]$, a species we also believe is formed via overall 2-electron oxidation of $[(TPB)^{57}Fe(N_2)][Na(Et_2O)_x]$ and release of H_2. Although this spectrum has been fit assigning this species to $[(TPB)Fe][BAr^F{}_4]$, there are a variety of other S = 3/2 complexes on the TPB manifold that have similar Mössbauer parameters and may also be reasonable assignments. The remaining component, $[(TPB)Fe{\equiv}N\text{-}NH_2][BAr^F{}_4]$, displays hyperfine parameters most similar to $[(TPB)^{57}Fe(N_2)][Na(Et_2O)_x]$, although with a smaller isomer shift value. In the related $(SiP_3)Fe$ system, functionalization of a bound N_2 ligand with silyl electrophiles was similarly found to reduce the isomer shift value relative to the Fe-N_2 complex.[11] At present, we cannot rule out the solution shown in Figure S7B and further studies will be needed to distinguish between these two simulations. Summarizing, Mössbauer spectroscopy indicates that at least three major Fe-

containing species are generated upon protonation of $[(TPB)^{57}Fe(N_2)][Na(Et_2O)_x]$ at low temperatures in Et_2O, at least under the conditions needed to collect these Mössbauer spectra.

Collection and Interpretation of ENDOR Data. 'Q-band' ~35 GHz continuous wave (CW) electron paramagnetic resonance (EPR) spectra were collected at 2 K with a helium immersion dewar on a modified Varian E-110 by the digitization of the RC-smooth output signal under 'rapid adiabatic' and with 100 kHz field modulation (2.0 G modulation amplitude).

Pulsed Q-band EPR and electron nuclear double resonance (ENDOR) experiments were executed on a custom-built instrument previously described at 2 K with data acquisition preformed with the SpecMan software package (specman4epr.com) in conjunction with a Spin-Core PulseBlaster ESR_PRO 400 MHz word generator and Agilent Technologies Acquiris DP235 500MS/sec digitizer. ENDOR spectra were collected using either the Davies microwave '3 pulse' sequence ($\pi - T - \pi/2 - \tau - \pi - \tau$ - echo), '3 pulse' Mims ($\pi/2 - T - \pi/2 - \tau - \pi/2 - \tau$ - echo), or a '4 pulse' refocused Mims, termed a ReMims, ($\pi/2 - \tau_1 - \pi/2 - T - \pi/2 - \tau_2 - \pi - \tau_2 - echo$), where the RF pulse is applied during time T and the RF frequency is randomly hopped in each pulse sequence. A blindspot occurs at $A\tau = n$ (where $n = 0, 1, 2, \ldots$) for a Mims sequence, however, the ReMims allows for ENDOR collection of weakly coupled nuclei with no blindspots.

The ENDOR spectrum from a nucleus with spin of $I = ½$ (^1H, ^{15}N, ^{31}P) and from the $m_s = \pm ½$ electron-spin manifold exhibits a doublet at frequencies,

$$\nu_{\pm} = \left| A/2 \pm \nu_n \right| \qquad (1)$$

where ν_n is the nuclear Larmor frequency and A is the hyperfine coupling. When $I \geq 1$ (^{11}B, ^{14}N), a nuclear quadrupole interaction (P) introduces further splitting of the $\nu_{\pm}$ manifolds.

$$\nu_{\pm,m_I} = \left| \nu_n \pm \frac{3P(2m_I - 1)}{2} \right| \qquad (2)$$

All ENDOR spectral simulations were performed in Matlab with the EasySpin v5 (easyspin.org) toolbox.

The absolute hyperfine coupling signs and spin density signs are obtained through the Pulsed ENDOR SaTuration and REcovery protocol. Extensively described elsewhere,[12] the PESTRE protocol determines the absolute sign of $\rho = A/g_n$ (where g_n is the nuclear g value for a given nuclide) through three different stages of repeating Davies ENDOR sequences. In the first stage, with no RF frequency applied during the Davies sequence, a baseline (BSL) of the electron spin echo (ESE) response is measured. Next, the ENDOR response is saturated by now applying an RF pulse during the Davies sequence during the second stage. Lastly, the RF pulses are turned off in the third stage and the ESE is allowed to relax back to the BSL to measure the DRL response. The two distinct relaxation possibilities, a positive response of a relaxtion from above

to down to the BSL, or a negative response from below up to the BSL is the δDRL response (δDRL = DRL - BSL). The positive or negative sign of the δDRL determines the spin density sign and therefore the absolute hyperfine sign.

VMT-PESTRE

Based on the original PESTRE protocol, stages of Davies microwave pulse sequences are employed with and without an fixed applied RF (ENDOR) frequency to observed saturation and relaxation behavior (termed δDRL) of a given ENDOR response. VMT-PESTRE compares the relaxation behavior of the ENDOR response as the 'mixing time' is lengthened, eventually inducing a 'flip' of the relaxation response, confirming the initial, sometimes weak, relaxation observation of 'fast' mixing times.

ESEEM

Electron spin echo envelope modulation (ESEEM) spectra were collected using a 3 microwave pulse sequence ($\pi/2$ - τ - $\pi/2$ - ΔT - $\pi/2$ - τ - *echo*) with phase cycling. Simulations of the ESEEM results were performed using the MATLAB based OPTESIM software package.[13] The spin Hamiltonian for interaction of the Fe(I) electron spin (S=1/2) with the remote ^{14}N nuclear spin (I = 1) is formulated with a nuclear Zeeman term, a hyperfine (hf, $\boldsymbol{A}$) and a nuclear quadrupole (nqi) term, as follows:

$$H = g_n\beta_n\vec{S}\cdot\vec{B} + h\vec{S}\cdot\mathbf{A}\cdot\vec{I} + \vec{I}\cdot\mathbf{Q}\cdot\vec{I}$$

In this expression, g_n is the nuclear g-value, β_n is the nuclear magneton, S is the electron spin operator, I is the nuclear spin operator, **A** is the hf coupling tensor, and **Q** is the nqi tensor. The hf tensor has the principal components, $\mathbf{A} = [A_{xx}\ A_{yy}\ A_{zz}]$, and is composed of an isotropic part, $a_{iso} = \frac{1}{3}\sum_i A_{ii}$, and a dipolar part, $T_{dip} = A - A_{\mathrm{iso}}$. The nqi tensor has the principal components, $\mathbf{Q} = [Q_{xx}\ Q_{yy}\ Q_{zz}]$, and is defined by the nuclear quadrupole coupling constant, e^2qQ/h, and the electric field gradient asymmetry parameter, η. In its principal axis system (PAS), **Q** is related to e^2qQ/h and η by the following expressions:

$$Q_{zz} = \frac{e^2qQ}{2I(2I-1)h}$$

$$\eta = \frac{Q_{xx} - Q_{yy}}{Q_{zz}}$$

The orientation between the nqi tensor PAS and the hf tensor PAS is defined by the Euler angles, $[\alpha_Q, \beta_Q, \gamma_Q]$. For a system with more than one coupled nucleus, the orientation of the hf PAS of each nucleus relative to the g-tensor reference frame is defined by the Euler angles, $[\alpha_{\mathrm{A}}, \beta_{\mathrm{A}}, \gamma_{\mathrm{A}}]$. The OPTESIM optimization uses the Nelder-Mead simplex method.

$^{14/15}N$ ENDOR: Full interpretation of the ENDOR data is convoluted by the ^{11}B ν- feature and harmonics described in the caption of Figure 5 of the main text. The incomplete tensor of **2-(^{14}N)** obtained from ENDOR spectroscopy was better estimated from 'Q-band' ESEEM spectroscopy (Figure S9). The single-field three microwave pulse ESEEM spectrum of **2-(^{14}N)** is well simulated with a single ^{14}N tensor of A = [4.34, 7.18, 6.22] MHz and quadrupole parameters of e^2qQ/h = 1.76 and η = 0.64. The hyperfine tensor is within reasonable agreement with the two principle hyperfine values obtained by ENDOR spectroscopy. As there is no orientation assignment of the ESEEM hyperfine tensor **A** with respect to **g** from the single field position, it is not known whether the maximum hyperfine coupling from the ESEEM simulation is not observed by ENDOR spectroscopy or is a slight overestimation as an artifact of high-frequency ESEEM. However, the e^2qQ/h = 1.76 quadrupole parameter is equivalent to an ENDOR quadrupole splitting of $P_{max} = 2[e^2qQ/(4I(2I-1)] = 0.88$ MHz, in excellent agreement with the observed P_2 = 0.90 MHz. Additionally, the ESEEM simulation estimates **P** rotated away from **A** as described an Euler angle, α = 60°.

^{11}B ENDOR: An unusually large coupling of 21 MHz is observed for **1** which decreases to 9 MHz upon protonation to form **2** coupled with a decrease in 2s ^{11}B unpaired orbital spin density from 0.40% to 0.17% (Figure S10). This observation is also consistent with the assignment of **2** as a hydrazido(2-) species, as an increased Fe-N bond order would be accompanied by an increased Fe-B distance, as observed in other (TPB)Fe≡NR species such as [(TPB)Fe≡N-Ad][BAr^F_4]. The decrease in coupling constant, although not explicitly required by an increase in the Fe-B distance, is fully consistent with a longer Fe-B interaction. Based on the original PESTRE protocol,[12] stages of Davies microwave pulse sequences are employed with and without an fixed applied RF (ENDOR) frequency to observed saturation and relaxation behavior (termed δDRL) of a given ENDOR response. VMT-PESTRE compares the relaxation behavior of the ENDOR response as the 'mixing time' is lengthened, eventually inducing a 'flip' of the relaxation response, confirming the initial, sometimes weak, relaxation observation of 'fast' mixing times. As shown in Figure S11, the ν_+ responses of the ^{11}B nuclei switches from a positive δDRL to a negative δDRL response, indicated by an downward pointing arrow for the ΔVMT-δDRL ('fast' to 'long' mixing time). This is typical of a nuclei with negative spin density and a negative A as $\rho \propto A/g_n$ ($g_n >$ for ^{11}B, ^1H, $g_n <$ ^{14}N). The ν_- yields the anticipated opposite VMT-PESTRE response (negative δDRL to positive δDRL).

Figure S1. 10 K EPR spectrum of [(TPB)Fe≡N-NH_2][BAr^F_4] (**2**).

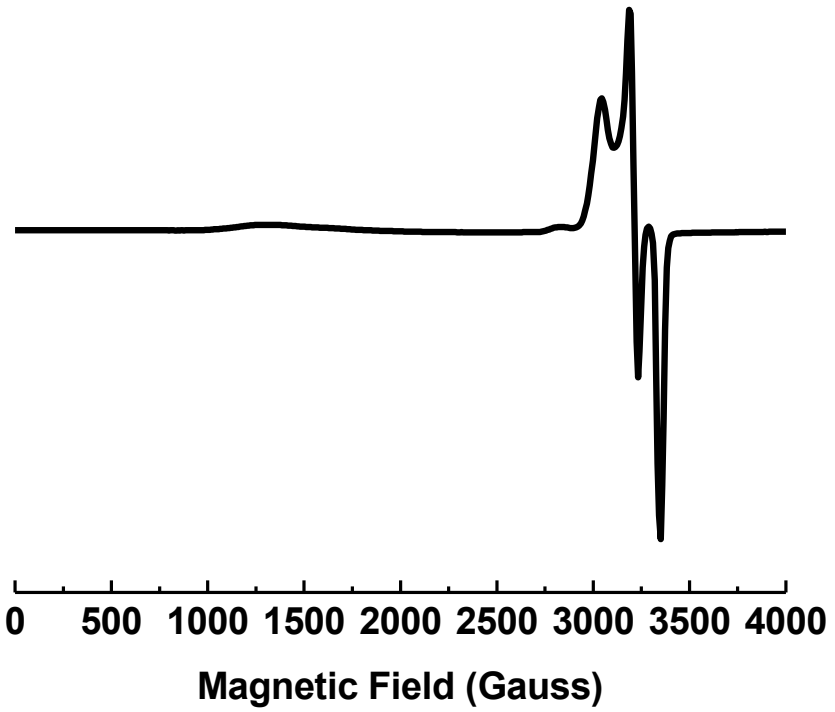

Conditions: 2-MeTHF, 10 K, microwave frequency 9.4 GHz, microwave power, 20.313 mW.

Figure S2. 77 K EPR spectrum of the addition of 1 equivalent of $HBAr^{F}_{4} \cdot 2\ Et_2O$ to complex **1**.

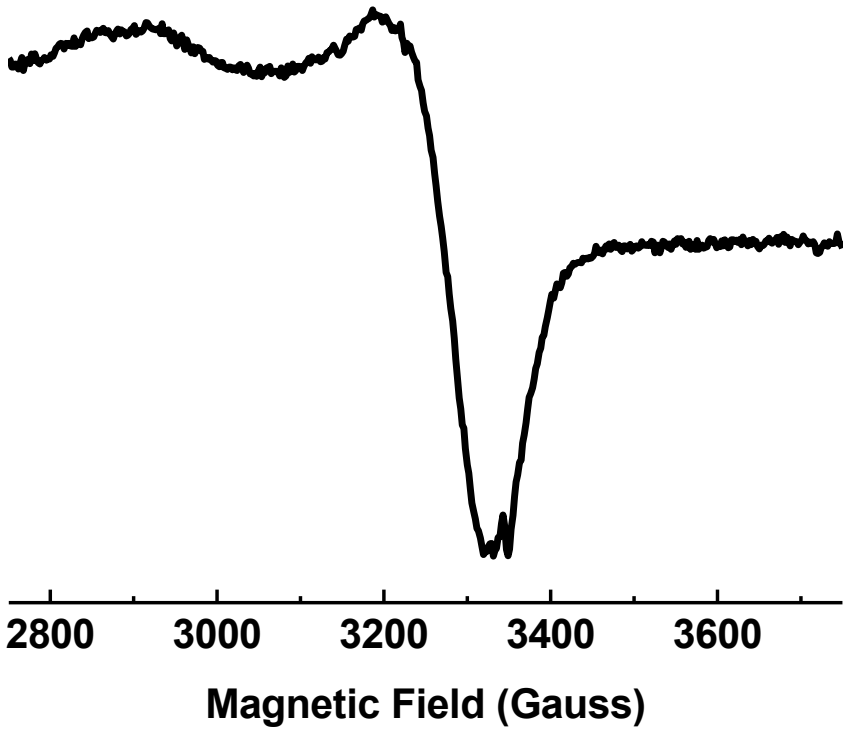

Conditions: 2-MeTHF, 77 K, microwave frequency 9.4 GHz, microwave power, 20.313 mW.

Figure S3. XRD Structure of [(TPB)Fe≡NAd][BAr^F_4].

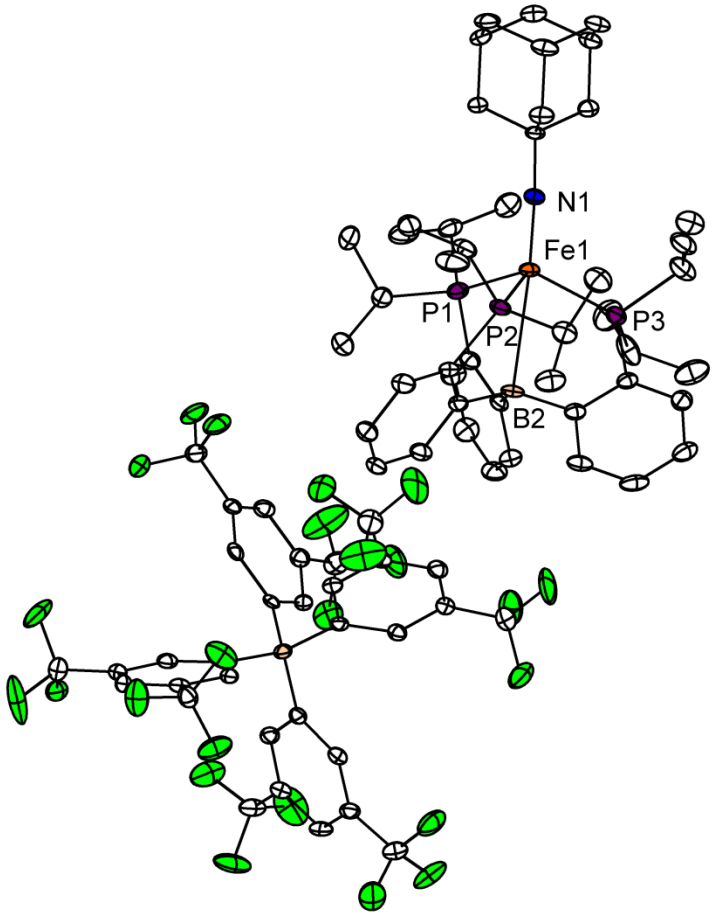

Note that hydrogens have been removed for clarity. Selected bond lengths (Å) and angles (°): Fe(1)-N(1) = 1.660(2), Fe(1)-P(1) = 2.3098(9), Fe(1)-P(3) = 2.3805(10), Fe(1)-P(2) = 2.3893(9), P(1)-Fe(1)-P(3) = 103.85(3), P(1)-Fe(1)-P(2) = 110.10(4), P(3)-Fe(1)-P(2) = 113.50(3).

Figure S4. Mössbauer spectra of [(TPB)Fe≡N-NH_2][$BAr^F{}_4$], **2**, at 80 K.

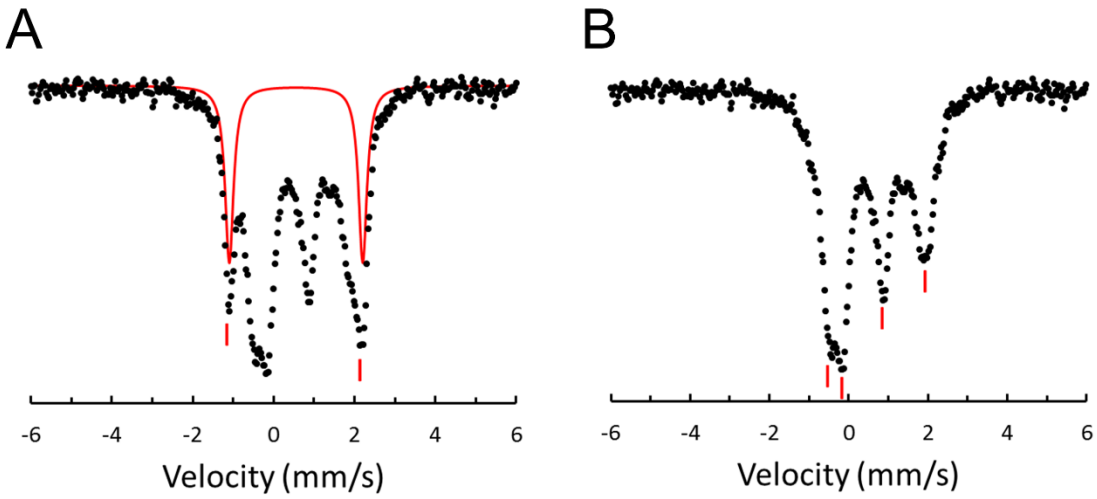

(A) 80 K ^{57}Fe Mössbauer spectrum obtained by low temperature protonation of [(TPB)Fe(N_2)][Na(Et_2O)$_x$] . The presence of (TPB)Fe(N_2) is highlighted with the red notches. The red trace shows a 19% (TPB)Fe(N_2) component. (B) Spectrum obtained by subtracting out 19% (TPB)Fe(N_2) from the spectrum shown in (A).

Figure S5. Mössbauer spectra of (TPB)Fe(N_2), [(TPB)Fe][$BAr^F{}_4$], and [(TPB)Fe(N_2)][$Na(Et_2O)_x$] at 80 K.

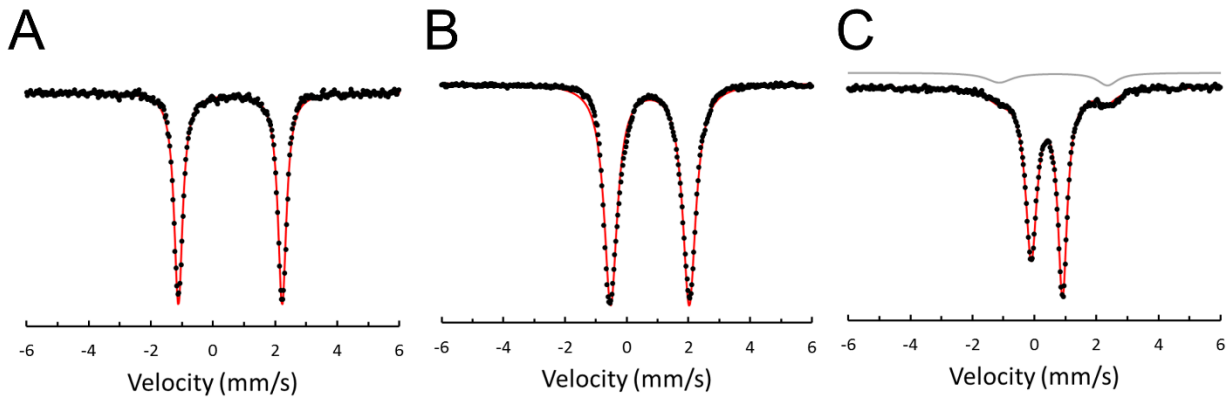

^{57}Fe Mössbauer spectra of (A) (TPB)Fe(N_2), (B) [(TPB)Fe][$BAr^F{}_4$], and (C) [(TPB)Fe(N_2)][$Na(Et_2O)_x$]. Spectra were collected on dilute frozen solutions (5 mM, Et_2O) in the presence of a 50 mT applied field applied parallel to the propagation of the gamma beam. The spectrum of [(TPB)Fe(N_2)][$Na(Et_2O)_x$] contains a 10% impurity of (TPB)Fe(N_2) that was likely generated during the brief exposure of the sample to air/water prior to immersion in liquid nitrogen.

Figure S6. Mössbauer spectra obtained on [(TPB)Fe(N_2)][Na(Et_2O)$_x$] under the listed conditions.

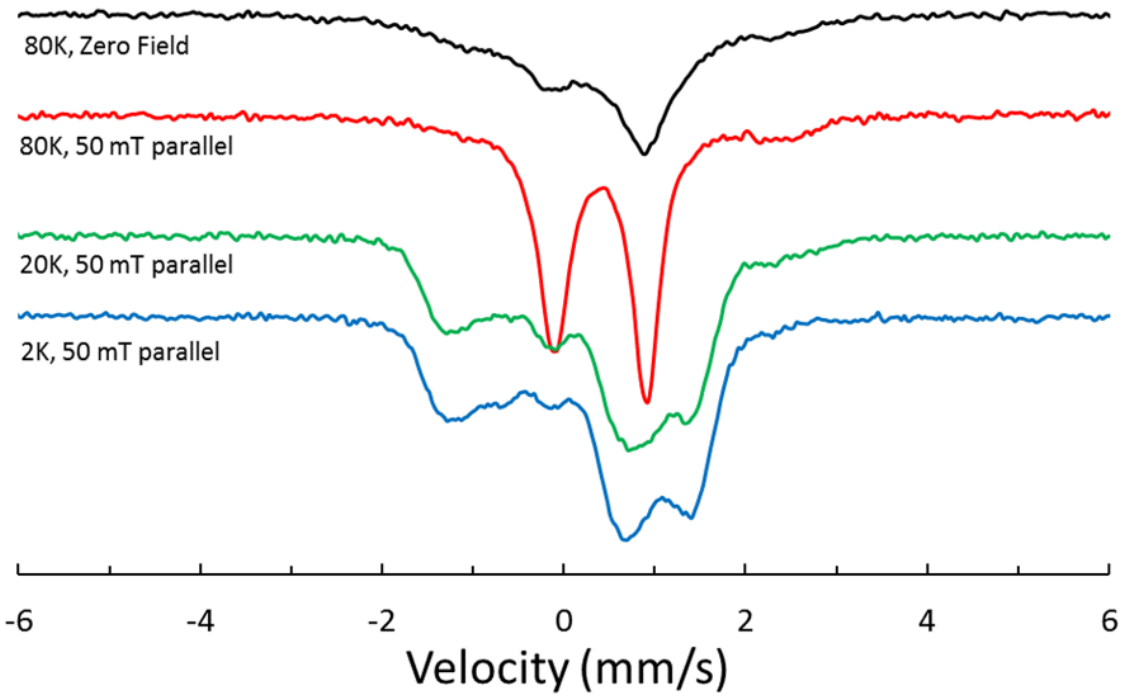

Figure S7. Considered fits to the Mössbauer spectrum of [(TPB)Fe≡N-NH_2][$BAr^F{}_4$], **2**, at 80 K.

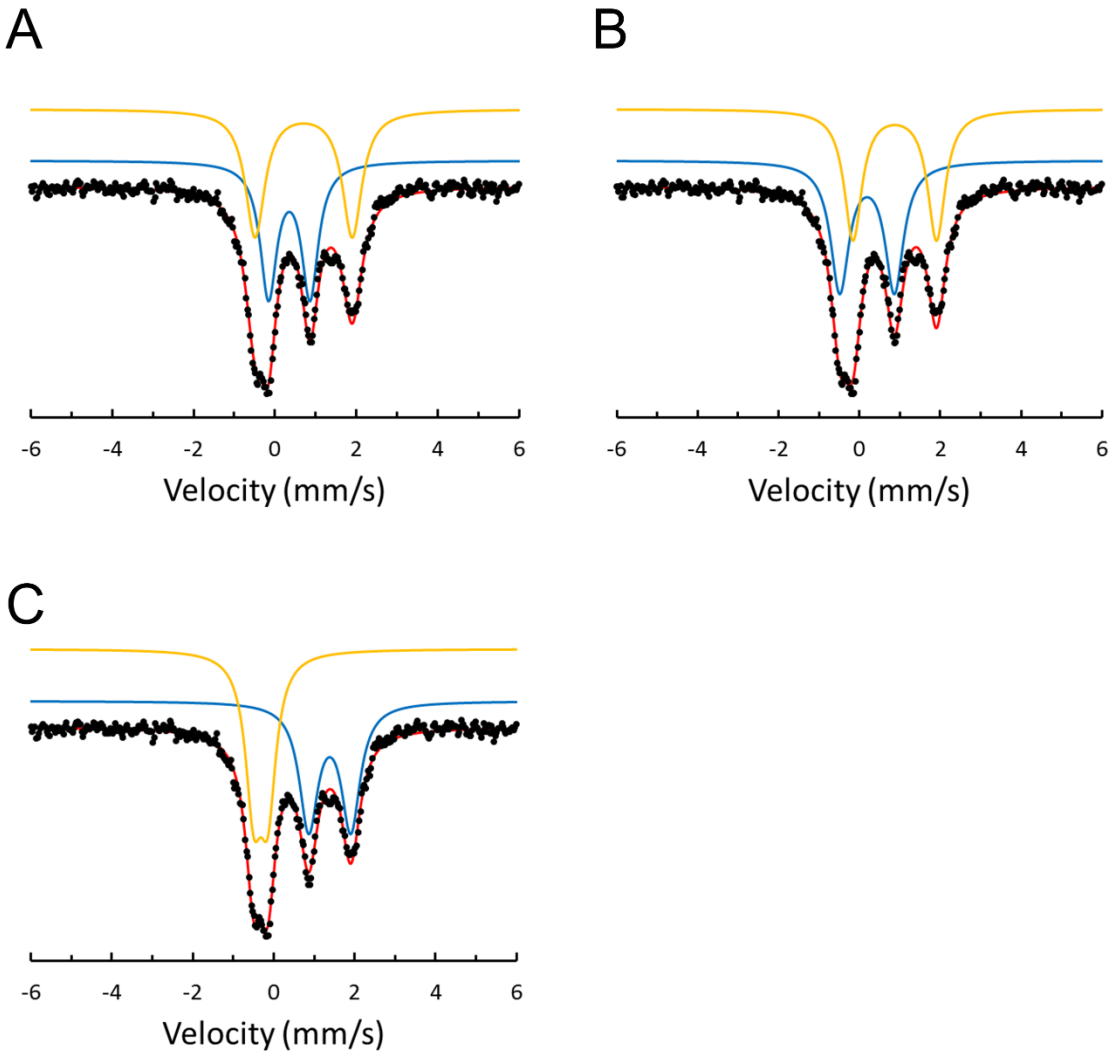

Spectral simulations of the two remaining Fe components after subtraction of the signal from (TPB)Fe(N_2). Data is shown in black dots, the combined simulation is shown as a red line, and the two simulated components are offset and shown as blue and yellow lines.

Figure S8. Depiction of the ENDOR modeled structure of [(TPB)Fe≡N-NH_2][$BAr^F{}_4$], **2**, and the orientation of hyperfine coupling tensors with respect to **g**.

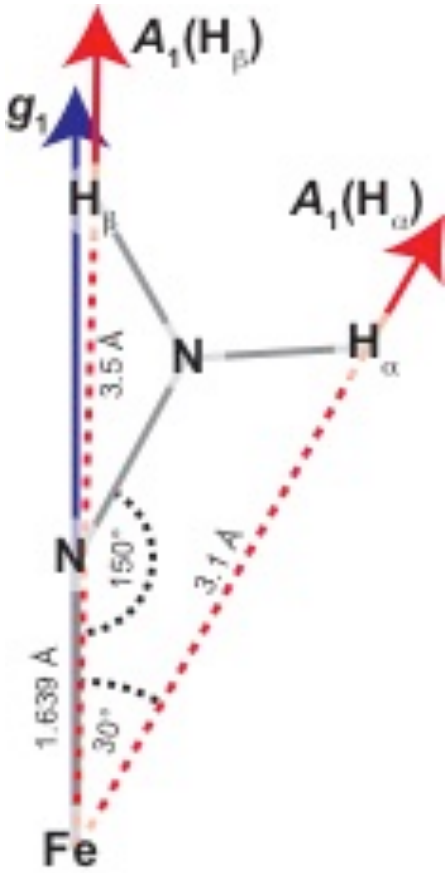

Figure S9. Three-pulse ESEEM waveform and FT spectrum for [(TPB)Fe≡N-NH_2][$BAr^F{}_4$], **2**.

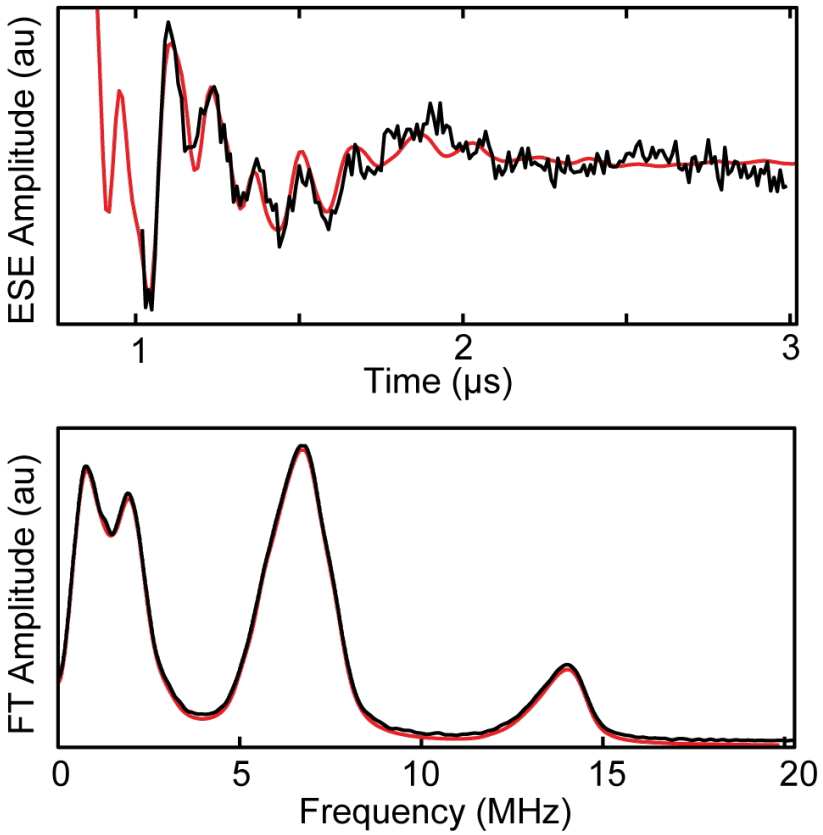

Three-pulse ESEEM waveform (top) and FT spectrum (bottom) for **2** complex with simulations (red lines). Simulation Parameters: **A** = [4.34, 7.18, 6.22] MHz, e^2qQ/h = 1.74 MHz, η = 0.64. The quadrupole tensor is rotated with respect to the hyperfine tensor with an Euler angle of α = 60°. Spectral Parameters: mw frequency = 35.388 GHz, 12059 G, τ = 680 ns, T_0 = 250 ns, ΔT = 10 ns. τ was selected to maximize the ^{14}N ESEEM response.

Figure S10. ^{11}B ENDOR Spectrum of [(TPB)Fe≡N-NH_2][BAr^F_4], **2**.

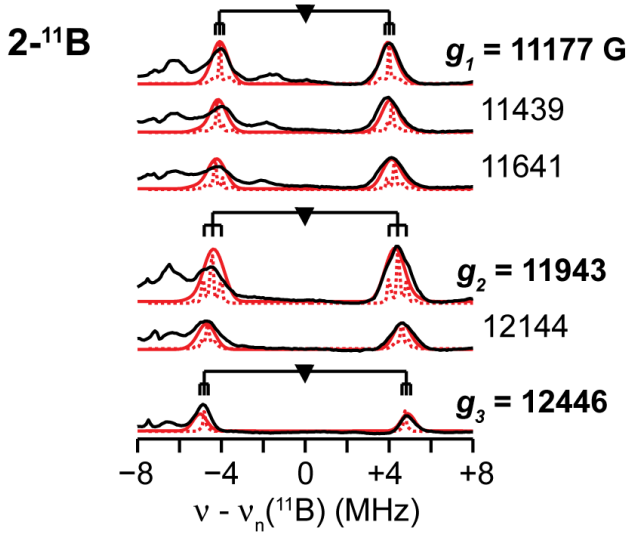

^{11}B Q-band Davies ENDOR of **2**, black with simulated (red solid) **A**(2-^{11}B) = [10, 8.3, 8.0] MHz, ENDOR lw = 0.7 MHz (fwhm). The field-dependent linewidths can be treated as reflecting variation in unresolved quadrupole splitting (P_{max} = 0.30 MHz), as shown by a simulation with a narrow ENDOR lw = 0.05 MHz (fwhm) shown in red.

Figure S11. VMT-PESTRE of [(TPB)Fe≡N-NH_2][$BAr^F{}_4$], **2**, at g_2.

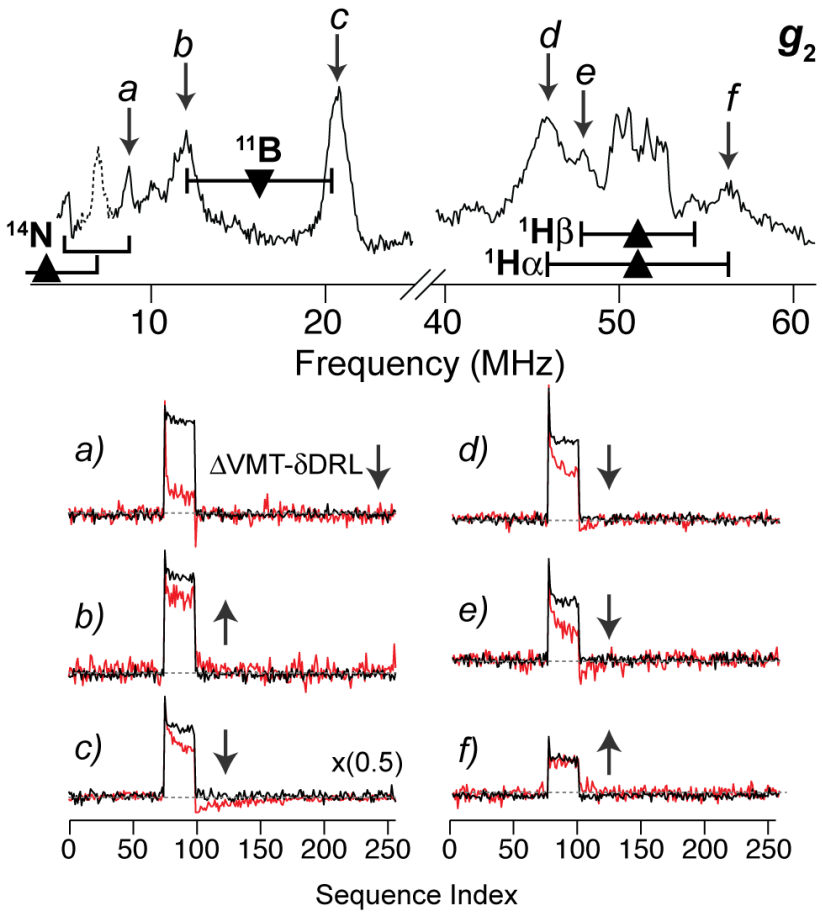

Q-band Davies ENDOR of **2** (top) at g_2. VMT-PESTRE traces at fixed RF frequencies: a) 8.71, b) 12.00, c) 20.80, d) 45.80, e) 47.90, f) 56.3 MHz. Up or down pointing arrows indicate the direction of change for the δDRL (ΔVMT-δDRL) response going from 'fast' to 'slow' mixing times. All traces are Davies ENDOR sequences of $\pi - T_{RF} - t_{mix} - \pi/2 - \tau - \pi -$ echo, where $\pi/2$ = 100 ns; τ = 600 ns; T_{RF} = 60 μs; t_{mix} = 5 μs (black) *or* 10,000 μs (red); repetition time = 20 ms. Sequence index: RF off (1 – 75), RF on (76 – 100), RF off (101 – 256).

Figure S12. Davies ENDOR segments from Figures 4 and 5 on an absolute RF scale to detail ^{31}P couplings.

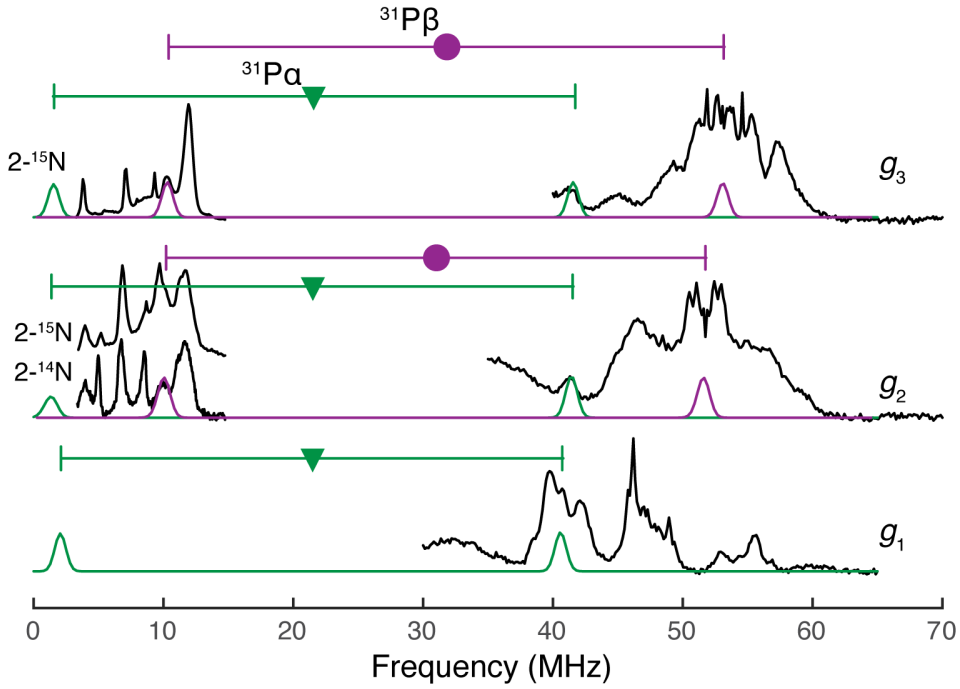

The ν_- of the ^{31}Pα (green) (A = [43, 42, 40] MHz) is not observable due to the low frequency of this transition. Additionally, the ν_+ of ^{31}Pα (A = [N/A, 61, 64] MHz) is obscured by the solvent proton (^{1}H > 4 MHz) at both g_2 and g_3.

Figure S13. M06L/TZVP(Fe)/SVP(P,N,B)/6-31G(C, H) optimized structure of $[(TPB)Fe(HNNH)]^{+}$.

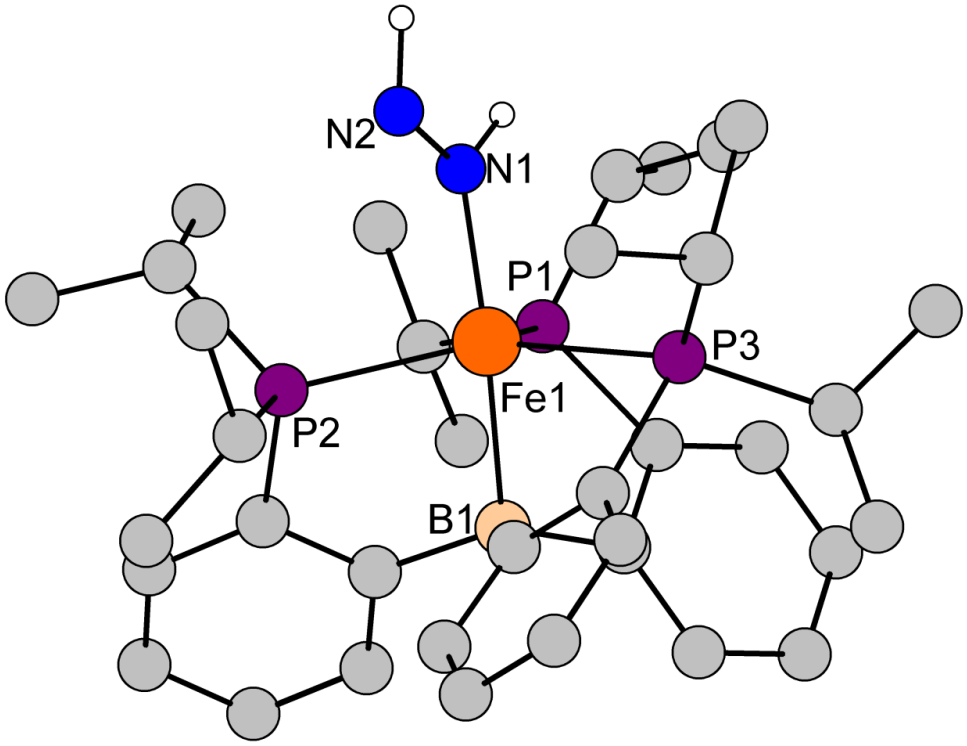

Selected bond lengths (Å) and angles (°): Fe1-N1 = 1.907, N1-N2 = 1.267, Fe1-P1 = 2.383, Fe1-P2 = 2.301, Fe1-P3 = 2.294, Fe1-B1 = 2.243, P1-Fe1-P2 = 107.42, P2-Fe1-P3 = 149.37, P3-Fe1-P1 = 98.61.

Figure S14. M06L/TZVP(Fe)/SVP(P,N,B)/6-31G(C, H) optimized structure of $[(TPB)Fe(HNNH)]^{+}$ with spin density plotted with an isovalue of 0.006.

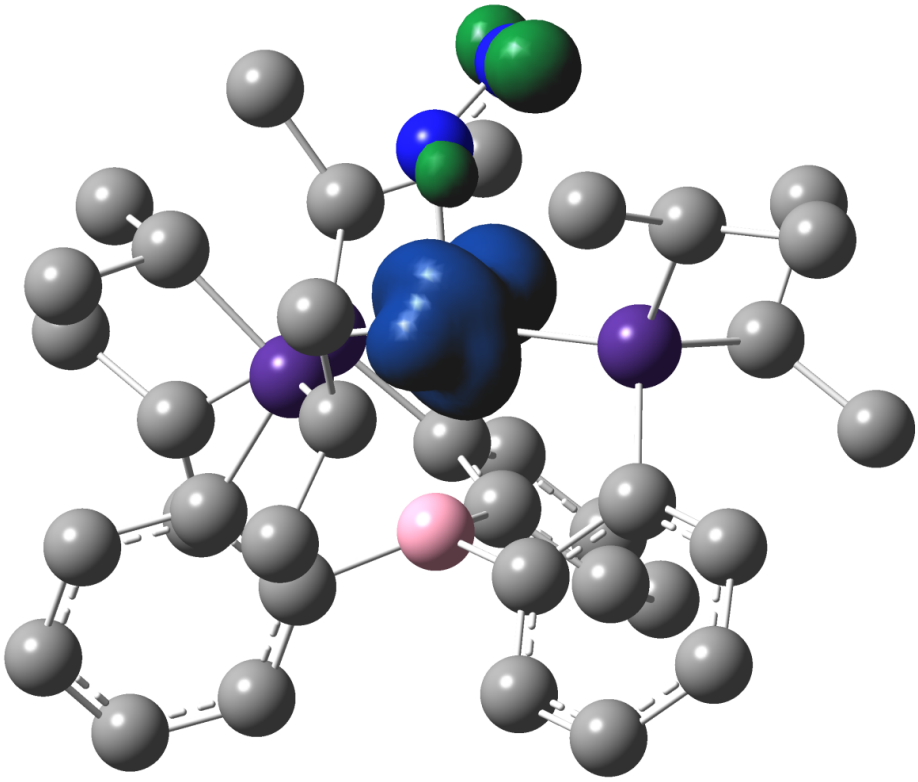

Figure S15. Comparison and evolution of EPR spectra associated with addition of acid to **1** at -136 °C and -78 °C.

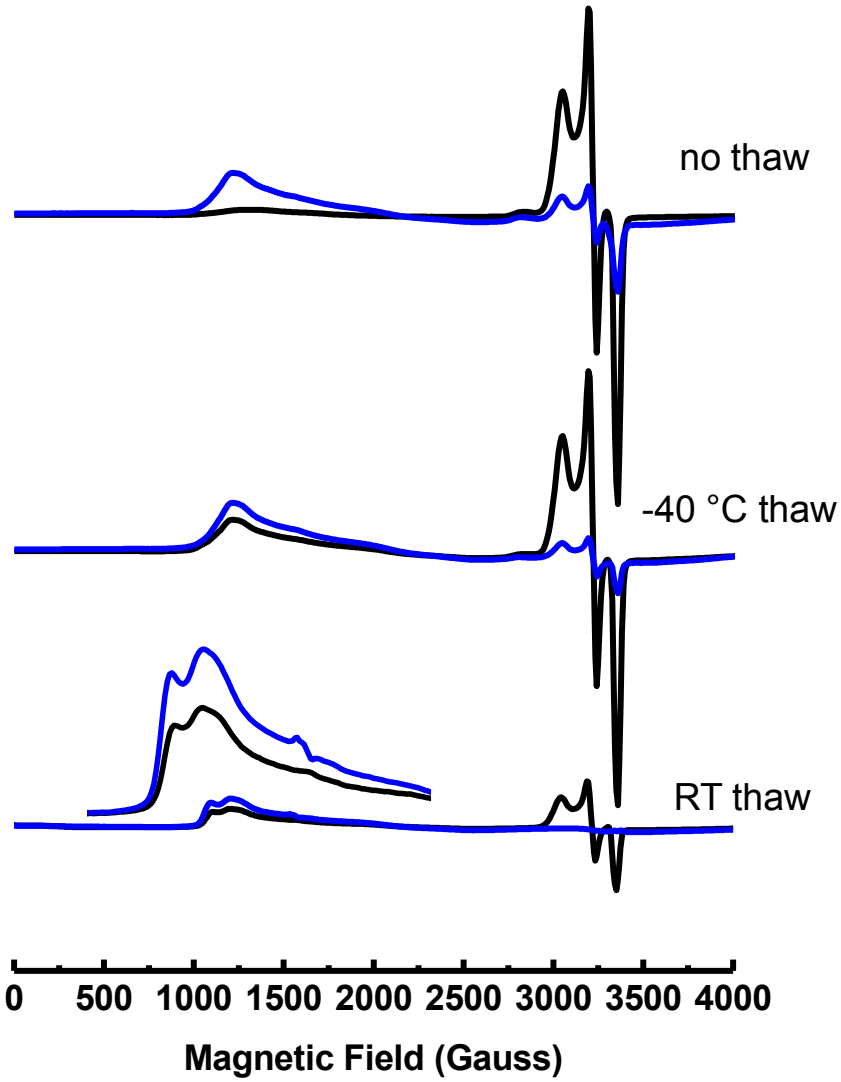

-78 °C preparation in blue, -136 °C preparation in black, spectra drawn to scale. All spectra recorded at 10 K.

Table S1. Tabulated Mössbauer parameters obtained by simulation of spectra shown in Figure S5.

(mm/s)	[(TPB)Fe(N_2)][Na(Et_2O)$_x$]	(TPB)Fe(N_2)	[(TPB)Fe][$BAr^F{}_{24}$]
δ	0.40	0.56	0.75
ΔE_Q	1.01	3.34	2.55
Γ_L	0.45	0.33	0.52
Γ_R	0.37	0.33	0.52

Table S2. Tabulated parameters obtained by the three simulations shown in Figure S7.

	Simulation A		Simulation B		Simulation C	
	Species 1	Species 2	Species 1	Species 2	Species 1	Species 2
δ	0.35	0.71	0.19	0.87	-0.32	1.382
ΔE_Q	1.02	2.39	1.35	2.06	0.35	1.04
Γ_L	0.50	0.58	0.55	0.53	0.49	0.56
Γ_R	0.50	0.58	0.55	0.53	0.49	0.56
Rel. Area	0.40	0.44	0.42	0.41	0.41	0.41

Table S3. DFT optimized energies [kcal/mol] for $[(TPB)Fe(N_2H_2)]^+$ congeners.

Complex	BP86	M06L
$S = 1/2$ $[(TPB)Fe{\equiv}N\text{-}NH_2]^+$	0	0
$S = 1/2$ $[(TPB)Fe(HNNH)]^+$	17.0	8.2

Table S4. Extended X-ray absorption fine structure (EXAFS) curve-fitting results for [(TPB)Fe≡N-NH_2][$BAr^F{}_4$], **2**.

	N	R (Å)	σ^2 (Å^2)	F-factor
Fe-P	1	2.279(5)	0.0021(2)	0.377
Fe-P	2	2.422(3)	0.0021(2)	
Fe-N	1	1.639(7)	0.0085(2)	
Fe-B	1	2.674(12)	0.0085(17)	

N, Coordination numbers, R, interatomic distances, σ^2 , Debye-Waller factors (the mean-square deviations in interatomic distance). The values in parentheses are the estimated standard deviations. The fit-error function is $F = \sqrt{\sum k^6(\chi(k)_{exp} - \chi(k)_{calcd})^2 / \sum \chi(k)_{exp}{}^2}$ where k is the photo-electron wave number. Note that including other single or multiple scattering paths collectively improves the fit less than 5% and are omitted to avoid over-parameterization of the data.

Table S5. Hyperfine coupling values (A) observed by ENDOR spectroscopy for **2**. All values in units of MHz.

	A_1	A_2	A_3
^{1}Hα	+18.0	+10.5	+8.0
^{1}Hβ	+11.5	+6.0	+4.5
^{15}Nα	N/A	+9.0	+8.0
^{14}Nα	N/A	–6.4	–5.7
^{14}Nα*	–4.34	–7.18	–6.22
^{11}B	8.0	8.3	10.0
^{31}Pα	43	42	40
^{31}Pβ	N/A	61	64

Table S6. Crystal data and structure refinement for [(TPB)Fe≡NAd][BAr^F_4].

Identification code	bac001	
Empirical formula	C78 H81 B2 F24 Fe N P3	
Formula weight	1658.82	
Temperature	100(2) K	
Wavelength	0.71073 Å	
Crystal system	Triclinic	
Space group	P-1	
Unit cell dimensions	a = 14.2869(9) Å	α= 98.092(2)°.
	b = 14.7963(9) Å	β= 109.786(2)°.
	c = 19.1431(11) Å	γ = 91.271(3)°.
Volume	3759.3(4) $Å^3$	
Z	2	
Density (calculated)	1.465 Mg/m^3	
Absorption coefficient	0.369 mm^{-1}	
F(000)	1706	
Crystal size		
Theta range for data collection	1.39 to 26.02°.	
Index ranges	-17<=h<=17, -18<=k<=18, -23<=l<=23	
Reflections collected	101295	
Independent reflections	14778 [R(int) = 0.0934]	
Completeness to theta = 26.02°	99.7 %	
Absorption correction	Semi-empirical from equivalents	
Max. and min. transmission	0.7458 and 0.6787	
Refinement method	Full-matrix least-squares on F^2	
Data / restraints / parameters	14778 / 960 / 994	
Goodness-of-fit on F^2	1.013	
Final R indices [I>2sigma(I)]	R1 = 0.0520, wR2 = 0.1114	
R indices (all data)	R1 = 0.1075, wR2 = 0.1334	
Largest diff. peak and hole	1.000 and -0.455 $e.Å^{-3}$	

Table S7. M06L/TZVP(Fe)/SVP(P,N,B)/6-31G(C, H) DFT Optimized coordinates [Å] for $[(TPB)Fe{\equiv}N\text{-}NH_2]^+$, **2**.

Fe	0.042100	-0.321600	-1.074300
P	-0.433100	1.899600	-0.770400
P	2.243600	-0.595200	-0.421900
P	-1.966100	-1.314100	-0.315900
N	0.280800	-0.886100	-2.660100
C	-1.220100	-2.057900	1.178300
C	2.433700	-2.402800	0.086900
H	1.447200	-2.659500	0.495700
C	-0.222900	-1.280500	1.826500
C	2.651100	0.414000	1.032800
C	-1.378000	2.451200	-2.292800
H	-0.648500	2.305300	-3.102500
C	-1.159400	1.230700	1.689700
C	1.708100	1.631800	2.896800
H	0.844800	1.951500	3.478600
C	-2.409300	-2.791500	-1.393400
H	-3.262100	-3.295100	-0.909400
B	0.054700	0.233300	1.427800
C	0.426500	-1.852400	2.944600
H	1.198900	-1.277000	3.452400
C	0.088100	-3.120600	3.419400
H	0.598000	-3.531400	4.286900
C	3.935900	0.828200	1.417500
H	4.810700	0.512100	0.858700
C	-0.916900	-3.860200	2.784000
H	-1.193000	-4.842400	3.156300
C	4.102700	1.655800	2.532200
H	5.097700	1.983800	2.818900
C	2.986100	2.060900	3.268700
H	3.111300	2.710500	4.131000
C	3.482800	-0.364300	-1.798300
H	3.117800	-1.093100	-2.539000
C	-1.888300	1.263800	2.892500
H	-1.661800	0.539700	3.674200
C	-1.480300	2.176100	0.688800
C	1.005300	3.122800	-0.638000
H	1.835000	2.482600	-0.306200
C	-3.626700	-0.603600	0.271300
H	-3.412400	0.456500	0.461300
C	-2.488000	3.130300	0.889300
H	-2.724400	3.866000	0.127600
C	-2.909300	2.200800	3.088200

H	-3.473600	2.203500	4.017200
C	-2.815500	-2.356900	-2.811500
H	-3.021900	-3.243900	-3.422100
H	-1.998800	-1.802500	-3.288400
H	-3.706600	-1.727400	-2.837100
C	-3.208300	3.133700	2.089800
H	-3.999500	3.862200	2.242600
C	-1.232100	-3.774300	-1.505300
H	-1.474700	-4.560000	-2.230100
H	-0.974500	-4.255300	-0.559000
H	-0.336900	-3.247000	-1.857500
C	-1.826100	3.931000	-2.278900
H	-1.786000	4.344800	-3.292800
H	-1.216300	4.572900	-1.637200
H	-2.863600	4.010600	-1.939100
C	3.342100	1.030500	-2.413400
H	3.989900	1.130100	-3.292000
H	3.629400	1.812600	-1.698600
H	2.307600	1.213400	-2.723800
C	-1.566600	-3.329100	1.668000
H	-2.346500	-3.910000	1.180000
C	1.415400	3.778200	-1.969500
H	2.429500	4.183400	-1.871500
H	0.759500	4.613700	-2.231400
H	1.423100	3.083000	-2.814100
C	-2.587700	1.550000	-2.561400
H	-3.111200	1.878500	-3.466900
H	-3.296700	1.612700	-1.725000
H	-2.296900	0.501700	-2.692000
C	2.679600	-3.310900	-1.126200
H	2.586100	-4.360700	-0.826100
H	3.680600	-3.176400	-1.550600
H	1.945600	-3.126800	-1.920000
C	0.786500	4.193000	0.442100
H	1.689400	4.809600	0.530300
H	0.582000	3.751500	1.421600
H	-0.049300	4.858800	0.193100
C	3.466600	-2.634600	1.196800
H	3.447400	-3.689400	1.497200
H	3.248400	-2.030600	2.082600
H	4.487500	-2.400000	0.875000
C	-4.759200	-0.691800	-0.762100
H	-5.650300	-0.205800	-0.348100
H	-5.030300	-1.731800	-0.978600
H	-4.523400	-0.191900	-1.705100
C	4.957700	-0.686700	-1.510100

H	5.492800	-0.801400	-2.460800
H	5.097700	-1.610300	-0.941600
H	5.448300	0.127300	-0.968900
C	-4.089300	-1.245400	1.587700
H	-5.017700	-0.761200	1.913900
H	-3.352000	-1.134100	2.386800
H	-4.299900	-2.315700	1.463800
C	1.505500	0.800200	1.777800
N	0.678000	-1.514300	-3.702600
H	0.679500	-1.051700	-4.610700
H	0.860300	-2.519600	-3.697500

Table S8. M06L/TZVP(Fe)/SVP(P,N,B)/6-31G(C,H) DFT Optimized coordinates [Å] for $[(TPB)Fe(HNNH)]^{+}$.

Fe	0.044400	-0.524300	-0.675200
P	-0.661500	1.748300	-0.807700
P	2.333900	-0.522200	-0.450200
P	-1.983900	-1.486900	-0.206400
N	0.077800	-0.726900	-2.571300
C	-0.938100	-2.055400	1.163400
C	2.911100	-2.255000	0.020600
H	2.029400	-2.678800	0.520000
C	0.069500	-1.132800	1.595000
C	2.687200	0.633800	0.915300
C	-1.708400	2.120200	-2.328800
H	-1.014600	1.996000	-3.176300
C	-1.201700	1.279300	1.707600
C	1.733000	2.068800	2.619900
H	0.867300	2.440800	3.165600
C	-2.364900	-3.033300	-1.199600
H	-3.113100	-3.614800	-0.636200
B	0.106800	0.459500	1.339700
C	0.987900	-1.610000	2.578400
H	1.767800	-0.942300	2.932700
C	0.868700	-2.869700	3.153100
H	1.551500	-3.170200	3.943000
C	3.968000	1.097700	1.257000
H	4.847400	0.710300	0.751100
C	-0.137400	-3.747900	2.722100
H	-0.238200	-4.729700	3.175800
C	4.127300	2.055900	2.263500
H	5.121000	2.412900	2.518300
C	3.006600	2.549200	2.937900
H	3.127600	3.297400	3.716700
C	3.350200	-0.094400	-1.954500
H	3.053000	-0.893600	-2.651000
C	-1.857100	1.320300	2.949300
H	-1.464600	0.743700	3.785600
C	-1.731800	2.036800	0.636700
C	0.606200	3.166500	-0.791900
H	1.525600	2.652300	-0.477700
C	-3.615100	-0.931900	0.579500
H	-3.473500	0.138500	0.776100
C	-2.888400	2.811000	0.798800
H	-3.296500	3.396900	-0.018900
C	-3.023900	2.077400	3.110000
H	-3.536100	2.089600	4.068700
C	-2.946200	-2.668500	-2.578400

H	-3.195200	-3.585400	-3.124200
H	-2.199800	-2.127600	-3.173500
H	-3.849600	-2.056600	-2.529000
C	-3.538700	2.818000	2.039500
H	-4.444000	3.404200	2.170400
C	-1.104000	-3.888700	-1.427300
H	-1.354900	-4.729100	-2.084800
H	-0.683200	-4.301500	-0.508400
H	-0.317400	-3.307600	-1.924400
C	-2.266600	3.566100	-2.374000
H	-2.132800	4.003400	-3.369100
H	-1.795700	4.239000	-1.653100
H	-3.341200	3.560900	-2.163100
C	2.905700	1.242900	-2.546400
H	3.382800	1.413400	-3.518700
H	3.181400	2.078000	-1.889700
H	1.819000	1.269700	-2.685300
C	-1.014400	-3.350000	1.718700
H	-1.789700	-4.033300	1.381400
C	0.880400	3.830900	-2.155600
H	1.864100	4.314700	-2.124600
H	0.147900	4.611100	-2.380900
H	0.893100	3.130800	-2.996600
C	-2.864100	1.123300	-2.477700
H	-3.453700	1.351200	-3.373400
H	-3.531500	1.200000	-1.609200
H	-2.528300	0.082200	-2.543200
C	3.181200	-3.116300	-1.223800
H	3.294600	-4.163100	-0.919600
H	4.106600	-2.824300	-1.732700
H	2.361800	-3.059200	-1.949800
C	0.296300	4.242000	0.260200
H	1.120000	4.966200	0.292200
H	0.180700	3.819300	1.261700
H	-0.622700	4.792000	0.023000
C	4.074700	-2.296700	1.018300
H	4.253100	-3.334200	1.326900
H	3.864500	-1.709300	1.918200
H	5.008000	-1.920400	0.583800
C	-4.832400	-1.107100	-0.339400
H	-5.717800	-0.709100	0.169700
H	-5.029700	-2.164100	-0.553200
H	-4.736100	-0.575200	-1.290100
C	4.878800	-0.128100	-1.804100
H	5.340100	-0.113500	-2.799200
H	5.242300	-1.021400	-1.288700

H	5.243900	0.754200	-1.269100
C	-3.865600	-1.645000	1.915700
H	-4.799800	-1.271400	2.351900
H	-3.062600	-1.465800	2.635800
H	-3.974400	-2.729500	1.783700
C	1.535200	1.102400	1.614400
N	0.696100	-1.586000	-3.267700
H	0.524200	-1.437200	-4.272600
H	-0.471600	-0.036500	-3.111300

Table S9. BP86/6-31G(d)(Fe,P,N,B)/6-31G(C,H) DFT Optimized coordinates [Å] for $[(TPB)Fe{\equiv}N\text{-}NH_2]^+$, **2**.

Fe	0.033511	-0.327788	-1.003814
P	-0.469167	1.897407	-0.790705
P	2.269808	-0.588519	-0.421092
P	-1.980504	-1.351651	-0.318695
N	0.262069	-0.866988	-2.580202
C	-1.225278	-2.098794	1.192438
C	2.510567	-2.411743	0.120449
H	1.543019	-2.650199	0.597118
C	-0.226902	-1.297929	1.836489
C	2.679097	0.440157	1.043692
C	-1.361470	2.477164	-2.371966
H	-0.544388	2.425939	-3.118777
C	-1.154471	1.241422	1.703299
C	1.722143	1.583015	2.964077
H	0.855986	1.876679	3.564834
C	-2.463048	-2.837061	-1.410453
H	-3.334989	-3.301892	-0.904922
B	0.059412	0.225451	1.406699
C	0.417146	-1.855755	2.979731
H	1.188156	-1.269095	3.488235
C	0.067562	-3.120217	3.483114
H	0.567445	-3.511328	4.373610
C	3.970110	0.859004	1.438462
H	4.852586	0.579279	0.862067
C	-0.934985	-3.879925	2.847992
H	-1.217359	-4.860029	3.240378
C	4.131325	1.648470	2.592570
H	5.129515	1.980904	2.888930
C	3.006029	2.009253	3.354964
H	3.127441	2.625154	4.250751
C	3.509756	-0.357146	-1.835878
H	3.130076	-1.096393	-2.571235
C	-1.834484	1.307329	2.945261
H	-1.578714	0.594915	3.736780
C	-1.519392	2.176095	0.692954
C	0.983262	3.157197	-0.622782

H	1.807501	2.509003	-0.272824
C	-3.662435	-0.628257	0.288856
H	-3.405731	0.417502	0.534305
C	-2.517884	3.148758	0.918398
H	-2.784009	3.878071	0.152370
C	-2.843275	2.265336	3.170770
H	-3.364425	2.294169	4.132106
C	-2.887859	-2.402544	-2.835952
H	-3.218479	-3.292248	-3.401684
H	-2.035458	-1.958114	-3.375603
H	-3.713384	-1.677883	-2.844755
C	-3.185469	3.182959	2.159467
H	-3.969944	3.924939	2.332847
C	-1.325218	-3.879456	-1.524503
H	-1.636908	-4.687337	-2.210284
H	-1.053081	-4.333790	-0.561065
H	-0.417956	-3.408217	-1.938722
C	-1.906016	3.932406	-2.330072
H	-1.987153	4.319247	-3.361672
H	-1.278063	4.632768	-1.760333
H	-2.919960	3.949464	-1.898677
C	3.375011	1.041945	-2.469604
H	4.020777	1.114645	-3.362455
H	3.684105	1.832402	-1.764982
H	2.335193	1.236158	-2.773897
C	-1.575976	-3.370714	1.705027
H	-2.357704	-3.967123	1.225735
C	1.429205	3.834773	-1.942996
H	2.414004	4.308258	-1.777758
H	0.735848	4.632547	-2.251462
H	1.541867	3.135739	-2.786014
C	-2.486744	1.526639	-2.824511
H	-2.890510	1.867924	-3.795019
H	-3.315603	1.541944	-2.096702
H	-2.133234	0.491326	-2.937455
C	2.690676	-3.366474	-1.081828
H	2.647873	-4.410525	-0.723685
H	3.661639	-3.234174	-1.588611
H	1.887149	-3.241911	-1.828429
C	0.735939	4.226116	0.469351

H	1.635255	4.864001	0.552504
H	0.547755	3.775580	1.454580
H	-0.118055	4.880655	0.222831
C	3.609318	-2.609007	1.189408
H	3.614490	-3.668144	1.503820
H	3.423296	-1.992564	2.082068
H	4.617284	-2.368668	0.813607
C	-4.797641	-0.625098	-0.762512
H	-5.671150	-0.107788	-0.326659
H	-5.122417	-1.647859	-1.017824
H	-4.536133	-0.097804	-1.692814
C	4.996575	-0.693391	-1.564055
H	5.534539	-0.712103	-2.528959
H	5.141318	-1.672740	-1.084562
H	5.482072	0.075077	-0.942488
C	-4.157593	-1.323673	1.579555
H	-5.097619	-0.840378	1.901019
H	-3.433109	-1.241071	2.402517
H	-4.376980	-2.393504	1.412337
C	1.520243	0.787704	1.805801
N	0.636885	-1.399663	-3.694312
H	0.636381	-0.849412	-4.561638
H	0.857010	-2.401405	-3.772874

Table S10. BP86/6-31G(d)(Fe,P,N,B)/6-31G(C,H) DFT Optimized coordinates [Å] for $[(TPB)FeHN{=}NH]^{+}$.

Fe	0.072100	0.055200	-1.185100
P	1.705100	-1.423100	-0.589900
P	-2.299800	-0.378300	-0.618100
P	0.843000	2.114600	-0.356400
C	-0.314300	2.478600	1.016200
C	-3.384500	1.154700	-0.303500
H	-2.679600	1.836100	0.208900
C	-0.661000	1.314900	1.766200
C	-2.314900	-1.435100	0.883200
C	2.997200	-1.704900	-1.970900
H	2.363500	-2.262700	-2.693100
C	1.433600	-0.416900	1.893400
C	-1.010900	-2.167300	2.805700
H	-0.110300	-2.104100	3.427200
C	0.666300	3.541800	-1.592000
H	0.929400	4.442000	-0.998900
B	-0.072300	-0.140000	1.391400
C	-1.511300	1.499500	2.890700
H	-1.810500	0.626300	3.481700
C	-1.987600	2.775500	3.254200
H	-2.641300	2.885600	4.127100
C	-3.345100	-2.334400	1.245400
H	-4.259700	-2.405300	0.650100
C	-1.638000	3.907400	2.491600
H	-2.017000	4.898200	2.765000
C	-3.201200	-3.155300	2.382200
H	-3.999100	-3.854900	2.654500
C	-2.029100	-3.076000	3.158100
H	-1.909100	-3.718400	4.038100
C	-3.147400	-1.340000	-2.027400
H	-2.895800	-0.718500	-2.912300
C	1.821400	-0.104700	3.226200
H	1.102900	0.394700	3.887000
C	2.405500	-1.045800	1.059500
C	0.951500	-3.185300	-0.391600
H	-0.096100	-2.965500	-0.106600
C	2.510100	2.462000	0.517500
H	2.384500	1.889600	1.456000
C	3.696400	-1.363100	1.543900
H	4.430600	-1.861300	0.906000
C	3.110800	-0.405400	3.708000
H	3.384000	-0.146300	4.737300
C	1.673900	3.434800	-2.766300
H	1.517200	4.277500	-3.465700

H	1.534800	2.499000	-3.339900
H	2.722800	3.473200	-2.429000
C	4.050000	-1.034600	2.866900
H	5.053700	-1.269900	3.237700
C	-0.777900	3.715400	-2.115100
H	-0.835900	4.629800	-2.735800
H	-1.507900	3.814700	-1.294600
H	-1.084900	2.859300	-2.738000
C	4.199500	-2.628700	-1.628600
H	4.673600	-2.971900	-2.568600
H	3.911200	-3.524800	-1.054500
H	4.969400	-2.079900	-1.059600
C	-2.516600	-2.741000	-2.215600
H	-2.956700	-3.227600	-3.106800
H	-2.714300	-3.390100	-1.343600
H	-1.427600	-2.680800	-2.364600
C	-0.798200	3.759800	1.369100
H	-0.535800	4.644000	0.777000
C	0.930500	-4.023000	-1.696000
H	0.294000	-4.913700	-1.536900
H	1.936300	-4.385600	-1.973100
H	0.506500	-3.476900	-2.557800
C	3.508700	-0.440000	-2.708400
H	3.897200	-0.731000	-3.703600
H	4.337600	0.039100	-2.163400
H	2.723300	0.323300	-2.858000
C	-3.822600	1.839300	-1.626600
H	-4.150100	2.873100	-1.407500
H	-4.672600	1.323000	-2.103100
H	-3.001800	1.891200	-2.361400
C	1.582200	-4.004100	0.765000
H	1.041300	-4.965600	0.856100
H	1.504400	-3.480300	1.730500
H	2.647400	-4.235600	0.583600
C	-4.577100	0.916900	0.656700
H	-5.077400	1.885000	0.852800
H	-4.243400	0.507400	1.624700
H	-5.331900	0.232000	0.232400
C	3.766600	1.920500	-0.194800
H	4.647800	2.083500	0.454300
H	3.964400	2.428000	-1.155300
H	3.683800	0.839100	-0.373500
C	-4.694800	-1.490600	-1.970000
H	-5.040600	-1.891500	-2.942800
H	-5.227900	-0.545000	-1.795400
H	-5.008900	-2.212700	-1.196500

C	2.689700	3.958100	0.884800
H	3.553500	4.051000	1.570300
H	1.811700	4.376000	1.406600
H	2.910000	4.579700	-0.002600
C	-1.127600	-1.318400	1.671600
N	-0.000300	-0.683900	-2.825800
H	0.596100	-1.162800	-3.523400
N	-0.540700	0.484000	-3.126100
H	-0.048500	0.959200	-3.911000

References Cited:

[1] Moret, M.-E.; Peters, J. C. *Angew. Chem. Int. Ed.* **2011**, *50*, 2063-2067.

[2] Brookhart, M.; Grant, B.; Volpe, A. F. *Organometallics* **1992**, *11*, 3920-3922.

[3] Chávez, I.; Alvarez-Carena, A.; Molis, E.; Roig, A.; Maniukiewicz, W.; Arancibia, A.; Arancibia, V.; Brand, H.; Manríquez, J. M. *J. Organomet. Chem.* **2000**, 601, 126-132.

[4] Weitz, I. S.; Rabinovitz, M. *J. Chem. Soc. Perkin* **1993**, 117-120.

[5] Stoll, S.; Schweiger, A. *J. Magn. Reson.* **2006**, *178*, 42-55.

[6] George, G.N., http://ssrl.slac.stanford.edu/exafspak.html.

[7] Ankudinov, A. L.; Ravel, B.; Rehr, J. J.; Conradson, S. D. *Physical Review B* **1998**, *58*, 7565-7576.

[8] Gaussian 03, Revision C.02, Frisch, M. J.; Trucks, G. W.; Schlegel, H. B.; Scuseria, G. E.; Robb, M. A.; Cheeseman, J. R.; Montgomery, Jr., J. A.; Vreven, T.; Kudin, K. N.; Burant, J. C.; Millam, J. M.; Iyengar, S. S.; Tomasi, J.; Barone, V.; Mennucci, B.; Cossi, M.; Scalmani, G.; Rega, N.; Petersson, G. A.; Nakatsuji, H.; Hada, M.; Ehara, M.; Toyota, K.; Fukuda, R.; Hasegawa, J.; Ishida, M.; Nakajima, T.; Honda, Y.; Kitao, O.; Nakai, H.; Klene, M.; Li, X.; Knox, J. E.; Hratchian, H. P.; Cross, J. B.; Bakken, V.; Adamo, C.; Jaramillo, J.; Gomperts, R.; Stratmann, R. E.; Yazyev, O.; Austin, A. J.; Cammi, R.; Pomelli, C.; Ochterski, J. W.; Ayala, P. Y.; Morokuma, K.; Voth, G. A.; Salvador, P.; Dannenberg, J. J.; Zakrzewski, V. G.; Dapprich, S.; Daniels, A. D.; Strain, M. C.; Farkas, O.; Malick, D. K.; Rabuck, A. D.; Raghavachari, K.; Foresman, J. B.; Ortiz, J. V.; Cui, Q.; Baboul, A. G.; Clifford, S.; Cioslowski, J.; Stefanov, B. B.; Liu, G.; Liashenko, A.; Piskorz, P.; Komaromi, I.; Martin, R. L.; Fox, D. J.; Keith, T.; Al-Laham, M. A.; Peng, C. Y.; Nanayakkara, A.; Challacombe, M.; Gill, P. M. W.; Johnson, B.; Chen, W.; Wong, M. W.; Gonzalez, C.; and Pople, J. A.; Gaussian, Inc., Wallingford CT, 2004.

[9] Gaussian 09, Revision A.1, Frisch, M. J.; Trucks, G. W.; Schlegel, H. B.; Scuseria, G. E.; Robb, M. A.; Cheeseman, J. R.; Scalmani, G.; Barone, V.; Mennucci, B.; Petersson, G. A.; Nakatsuji, H.; Caricato, M.; Li, X.; Hratchian, H. P.; Izmaylov, A. F.; Bloino, J.; Zheng, G.; Sonnenberg, J. L.; Hada, M.; Ehara, M.; Toyota, K.; Fukuda, R.; Hasegawa, J.; Ishida, M.; Nakajima, T.; Honda, Y.; Kitao, O.; Nakai, H.; Vreven, T.; Montgomery, Jr., J. A.; Peralta, J. E.; Ogliaro, F.; Bearpark, M.; Heyd, J. J.; Brothers, E.; Kudin, K. N.; Staroverov, V. N.; Kobayashi, R.; Normand, J.; Raghavachari, K.; Rendell, A.; Burant, J. C.; Iyengar, S. S.; Tomasi, J.; Cossi, M.; Rega, N.; Millam, J. M.; Klene, M.; Knox, J. E.; Cross, J. B.; Bakken, V.; Adamo, C.; Jaramillo, J.; Gomperts, R.; Stratmann, R. E.; Yazyev, O.; Austin, A. J.; Cammi, R.; Pomelli, C.; Ochterski, J. W.; Martin, R. L.; Morokuma, K.; Zakrzewski, V. G.; Voth, G. A.; Salvador, P.; Dannenberg, J. J.; Dapprich, S.; Daniels, A. D.; Farkas, Ö.; Foresman, J. B.; Ortiz, J. V.; Cioslowski, J.; Fox, D. J. Gaussian, Inc., Wallingford CT, 2009.

[10] Anderson, J. S.; Moret, M.-E.; Peters, J. C. *J. Am. Chem. Soc.* **2013**, *135*, 534.

[11] Lee, Y.; Mankad, N.P.; Peters, J.C.; *Nature Chemistry* **2010**, 2, 558-565.

[12] Doan, P. E. *Journal of Magnetic Resonance* **2011**, *208*, 76.

[13] Sun, L.; Hernandez-Guzman, J.; Warncke, K. *J. Magn. Reson.* **2009**, *200*, 21.